Red: referee#1

Green: referee#2

Blue: other upgrades introduced by the authors

Addition of a channel for XCO observations to a portable FTIR spectrometer for greenhouse gas measurements

F. Hase(1), M. Frey(1), M. Kiel(1), T. Blumenstock(1), R. Harig(2), A. Keens(2), and J. Orphal(1)

(1) Karlsruhe Institute of Technology (KIT), Institute for Meteorology and Climate Research (IMK-ASF), Karlsruhe, Germany

(2) Bruker Optik GmbH, Ettlingen, Germany

Correspondence to: Frank Hase (frank.hase@kit.edu)

Abstract

The portable FTIR (Fourier-Transform InfraRed) spectrometer EM27/SUN dedicated for the precise and accurate observation of column-averaged abundances of methane and carbon dioxide has been equipped with a second detector channel, which allows the detection of additional species, especially carbon monoxide. This allows an improved characterisation of observed carbon dioxide enhancements and makes the extended spectrometer especially suitable as a validation tool of ESA's Sentinel 5 Precursor mission, as it now covers the same spectral region as used by the infrared channel of the TROPOMI (TROPOspheric Monitoring Instrument) sensor. The extension presented here does not rely on a dichroic, but instead a

fraction of the solar beam is decoupled near the aperture stop of the spectrometer using a small plane mirror. This approach allows ~~to maintain~~ maintaining the camera-controlled solar tracker setup, which is referenced to the field stop in front of the primary detector. Moreover, the upgrade of existing instruments can be performed without alterating the optical setup of the primary channel and resulting changes of the instrumental characteristics of the original instrument.

1 Introduction

The ground based solar absorption FTIR (Fourier Transform InfraRed) technique is capable of providing highly reliable measurements of column-averaged CO_2 and CH_4 abundances. The TCCON (Total Carbon Column Observing Network, Wunch et al., 2011) is one of the established references for the validation of greenhouse gases measuring space sensors (Reuter et al., 2011; Wunch et al., 2011; Butz et al., 2011; Heymann et al., 2015; Inoue et al., 2016) and has also been used for e.g. model studies of greenhouse gases sources (Messerschmidt et al., 2013) and observation of local sources (Lindenmaier et al., 2014). Recently, several investigators demonstrated that portable low resolution FTIR spectrometers still allow surprisingly precise and accurate measurements of column-averaged greenhouse gas abundances (Petri et al., 2012, Gisi et. al. 2012, Frey et. al., 2015). Such devices are a promising supplement to the TCCON, for performing measurements at remote sites, for mobile applications (Klappenbach et al., 2015), and for observations of dedicated sources and sinks on regional and smaller scales (Hase et al., 2015).

In this work, we describe an instrumental extension of the system ~~described~~ introduced by Gisi et al. in 2012, comprised of a portable FTIR spectrometer based on a pendulum interferometer design and a camera-controlled solar tracker for ensuring proper alignment of the line of sight on the solar disc centre (Gisi et al., 2011). This spectrometer is available today as a standard device from the Bruker Optics company in Ettlingen under the model name EM27/SUN and is used by many working groups. The observing strategy follows the same approach demonstrated by TCCON: the near-infrared spectral bands of the greenhouse gases under study are co-recorded with the 1.27 um band of molecular oxygen. Thereby, the

column-averaged dry air mole fractions of a target species can be derived from the ratio of the target species column divided by the molecular oxygen column. This process takes advantage of our accurate knowledge of the dry air mole fraction of molecular oxygen and helps to reduce various error sources (Wunch et al., 2011). In addition, TCCON uses DC-coupled interferograms for improving the precision of the measurements and for quality flagging (Keppel-Aleks et al., 2007), which is also used for the portable spectrometers. The main difference is that the spectral resolution of the portable spectrometer is much lower: it provides double-sided interferograms with a maximum optical path difference (OPDmax) of 1.8 cm, while TCCON applies 45 cm or higher OPDmax. An instructive example of application is provided by Hase et al., 2015, where a set of five EM27/SUN spectrometers has been used for detecting the carbon dioxide enriched plume generated by the major city Berlin. The current EM27/SUN spectrometer offers a spectral coverage of about 5500 to 11000 cm^{-1}, slightly broader than the 6000 to 11000 cm^{-1} coverage used for the prototype described by Gisi et al., 2012. This still conservative choice has been made to avoid any compromise of measurement accuracy of the primary target species XCO_2 and XCH_4. Nevertheless, it would be highly desirable to add the capability of observing XCO, which is a ~~highly~~ valuable tool for the characterisation of sources connected to observed XCO_2 enhancements (Wunch et al., 2009). Moreover, an extension of the spectral coverage of the current EM27/SUN including the 2.3 μm region used by TROPOMI for the observation of carbon monoxide and methane would qualify the mobile spectrometer as a validation instrument for the Sentinel 5 Precursor mission. Here, we introduce an enhancement of the EM27/SUN by adding the capability of measuring XCO. In Section 2 we provide a summary of the basic design considerations, in Section 3 we describe the practical implementation of the extension, in Section 4 we present the characteristics of lamp and atmospheric solar spectra recorded with the dual-channel prototype, and in Section 5 we demonstrate the performance of the novel setup based on retrievals of atmospheric observations. Section 6 provides a summary of this study and an outlook towards planned future activities.

2 Design considerations for the XCO extension

The most straightforward approach for an XCO extension is obviously the replacement of the standard InGaAs diode covering 5500 – 11000 cm^{-1} by a detector element offering extended

spectral coverage. However, as the FTIR technique reconstructs the irradiated spectrum by performing a Fourier transformation of the measured interferogram, it is susceptible for characteristic interfering influences which degrade the recorded interferogram. Periodic sampling errors, nonlinear detector response, or radiation which is reflected back into the interferometer and modulated twice before detection (double passing), can all generate parasitic signals in the spectral domain. If the spectrum is confined to a sufficiently narrow region, the spectral perturbations can be detected (and corrected, if necessary) by the characteristic out-of-band artefacts they create, or they can be tolerated, if the parasitic spectral signal does not overlap with the real spectral signal. Increasing the spectral bandwidth does not only significantly increase the noise level of the spectrum, but is – more seriously – possibly harmful due to an insufficient level of control of the interfering influences mentioned above. The application of an extended InGaAs diode has been investigated (J. Hedelius et al., 2016), but resulted in a significant dependence of XCO_2 and XCH_4 on the overall signal level, probably due to a nonlinear detector response. This characteristic, which damages the reliability of the EM27/SUN primary data products, is highly undesirable and is not observed with the standard detector element.

An alternative approach is the use of an additional detector element for widening ~~up~~ the covered spectral region. This avoids the aforementioned problems, but requires either (1) the use of a sandwich detector element, ~~or~~ (2) alternating observations with different detectors, or (3) the distribution of the optical beam for feeding two separated detector elements at a time.

A sandwich detector comprised of two sensors with different spectral coverage is a delicate item of limited availability and considerably higher cost than a pair of separate detectors. Moreover, the increased number of stacked substrate interfaces promotes the occurrence of optical resonances, which generate undulations in the spectral domain ("channeling"), a ~~very nasty~~ highly undesirable feature from the viewpoint of quantitative spectral analysis of crowded spectral scenes as provided by the atmosphere.

The second option of alternating observations is accompanied by the drawback that species recorded in the two channels are not recorded simultaneously, it reduces the duty cycle of the measurement, and it requires an additional moving optical element in the detector branch of

the spectrometer, which gives rise to further risks, such as variable misalignment or complete failure of the unit.

Therefore, the third approach seems most promising. This approach has also been realized in the TCCON spectrometer operated by KIT near Karlsruhe: here, a dichroic allows simultaneous observation of the shortwave part of the spectral region (covering O_2, CO_2 and CH_4) together with either the longwave part (covering HF, N_2O, and CO) for achieving the same spectral coverage as the standard extended InGaAs diode used by other TCCON sites, or a spectral section in the mid-infrared spectral region as observed by spectrometers of the NDACC (Network for the Detection of Atmospheric Composition Change). The setup uses the same InGaAs detector as the EM27/SUN for the shortwave and a liquid-nitrogen cooled InSb detector for the longwave part of the spectrum. Further details and results achieved with this setup are provided by Kiel et al., 2015a, and Kiel et al., 2015b. The remaining drawback of the approach is that a specific dichroic is required, which complicates the alignment of the detector branch and generates undulations of the spectral sensitivity. The presence of undulations requires special attention in the processing of the spectra (Kiel et al., 2015a). In the case of the Karlsruhe high-resolution setup, any loss of the interferometric etendue (product of supported beam area and covered solid angle) permitted by the hardware configuration is undesirable in the InSb branch, because the NDACC-type of measurements ~~are~~ is performed with narrow optical filters at very high spectral resolution. Therefore, the choice of using a dichroic of good efficiency seems justified.

From the viewpoint of the EM27/SUN extension, the situation differs, as the interferometric etendue is deliberately limited by an adjustable iris acting as aperture stop. The detector uses only a small fraction of the etendue supported by the interferometer and solar tracker hardware, and a loss of signal can easily be compensated by a slight adjustment of the iris aperture. Therefore, in this case a wave front division seems the most appropriate approach. If finally this wave front division is executed near the aperture stop of the interferometer (defined by an adjustable iris), the characteristics of the existing detector branch remain unimpaired and with proper geometrical arrangement of the extension setup even the functionality of the camera-controlled solar tracker, which references the solar image to the position of the field stop aperture in front of the existing detector, is maintained.

3 Technical setup of the prototype

Figure 1 shows a schematic sketch of the partial beam decoupling and the longwave detector branch. Behind the adjustable iris aperture that defines the aperture stop of the system, an off-axis paraboloidal mirror is located, which offers 127 mm effective focal length and generates a solar image on the field stop in front of the existing detector element. Physically, the field stop is realized by a circular hole of 0.60 mm diameter in a thin disc of stainless steel. For partial decoupling of the beam, a plane mirror of 10 x 20 mm^2 size has been added. This mirror is located directly behind the off-axis paraboloid and accepts about 40% of the incoming converging beam. The deflection angle between the residual parent and reflected partial beam amounts to about 25 degrees and the deviation is chosen along the horizontal, so that the second detector element can be mounted next to the original detector.

The solar image is formed on a secondary aperture stop (0.80 mm diameter) in front of the additional detector element. The detector element used is a windowless extended InGaAs diode (cut off 4000 cm^{-1}) offering 1 mm^2 sensitive area. In a gap between the secondary field stop and the diode a wedged Germanium long pass filter is mounted, which shields the extended InGaAs diode from the spectral section already covered by the primary detector.

Figure 2 - 4 show close-up photographs of the dual-detector prototype. Figure 2 shows the small plane mirror just in front of the off-axis paraboloid. The mirror is glued with a two-component epoxy resin adhesive to its aluminium support. The bonding layer has been chosen to be thick and flexible enough to avoid deformation of the glass mirror due to temperature changes. The support structure allows fine adjustment of the direction of the beam reflected towards the secondary field stop. Figure 3 shows the image of an artificial source on the primary and secondary field stop. Figure 4 shows the detectors from the top. While the primary detector and preamplifier unit remain in the standard detector box, a short cable is used for operating the secondary detector outside of its box, which houses the preamplifier unit only. The secondary detector is mounted on a support structure, which in turn is solidly fixed to the primary detector box.

The alignment of the secondary fieldstop is performed by using an artificial external light source. The solar tracker is used for conveniently centring the image of the source on the primary fieldstop, the evaluation is performed with the camera of the solar tracker. The fine adjustment of the source image on the secondary field stop is performed by aligning the plane mirror, the evaluation is performed by eye with a magnifier. Finally, the position of the unit containing the wedged Germanium filter and the secondary detector element is adjusted with respect to the secondary field stop by searching for maximum signal level.

4 Characteristics of spectra recorded with the dual-channel prototype

Figure 5 (upper panel) shows a lamp spectrum recorded with the prototype. Both the primary and secondary channels are essentially free from channeling (we estimate the upper limit for the peak-to-peak amplitude in the primary channel to be 0.0005, in the secondary channel to be 0.0002) and ~~a proper definition~~ the desired separated spectral bandpass for each channel is achieved: The low wavenumber limit of the secondary detector results from the cut-off of the diode, its high wavenumber limit is defined by the Ge filter. Similarly, the low wavenumber limit of the primary detector is shaped by the diode cut-off, the high wavenumber limit is due to a Schott RG 830 longpass filter glass ~~which~~ that acts as entrance window of the spectrometer. Therefore, both detectors observe through this optical element and a further extension of the concept presented here towards lower wavenumbers would in addition to a suited detector element require a replacement of the entrance window (because the glass-based window becomes intransparent at a wavelength of about 3 µm). Finally, also a beamsplitter exchange would be needed, because the standard EM27/SUN is equipped with a Quartz substrate beamsplitter.

Figure 5 (lower panel) shows a raw solar spectrum recorded with the prototype. This spectrum reveals that the transition region between both channels coincides nicely with the opaque region created by the strong water vapour absorption between the atmospheric window regions H and K (we here refer to the established convention used in infrared astronomy: the H band covers 1.5 to 1.8 µm, the K band covers 2.0 to 2.4 µm). Close inspection of the zero baselines reveals a minor out-of band offset of the order of 0.015% for

the primary detector branch and no indication of out-of band signal for the secondary detector branch (below 0.0025%). The 1~~-sigma~~ σ signal-to-noise ratio in the peak of the primary channel is 13 000, the signal-to-noise ratio of the secondary channel reaches 20 000.

5 Results of atmospheric retrievals

To evaluate the instrument performance the modified spectrometer has been operated in parallel to a standard EM27/SUN for 6 days of measurements from mid of October to mid of November 2015 and on March, 18, 2016. Before the implementation of the extension, the selected spectrometer was operated side-by-side with the same standard EM27/SUN on various occasions. This allows us to check whether the modification of the spectrometer changed the oxygen column derived from the primary channel. We assume that the oxygen column is the most sensitive indicator for changes of the instrumental characteristics (especially instrumental line shape (ILS)), as instrumental error sources tend to cancel out in the final column-averaged abundances of the target gases. For this purpose, we selected seven days of measurements before the intervention was performed on the spectrometer and six days after the intervention. Table 1 ~~and Table 2~~ lists the measurements used in this study. The upper part of Table 1 lists the measurements taken between mid May and end the end of August side-by-side with the spectrometer ~~foreseen for the extension~~ used for the prototype (before modification) and a standard EM27/SUN used as reference. The lower part of Table 1 summarizes the measurements taken after implementation of the dual-channel extension, the measurements taken with the standard EM27/SUN reference (the same spectrometer as used previously), and the near- and mid-infrared measurements taken with the high-resolution FTIR spectrometer at Karlsruhe operated as part of the TCCON. The low-resolution interferograms used in this study passed the quality check implemented in our calibration routines (based on average DC level and DC variations during recording), the TCCON data used passed the standard quality flagging of the GGG software suite. For limiting airmass-dependent effects, data recorded at solar elevations below 15 degrees have been discarded. Note that the TCCON time series is somewhat sparser than for a typical TCCON site, due to alternating recording of high-resolution mid-infrared spectra.

The EM27/SUN side-by-side observations were performed on the roof terrace of our institute, at a distance of less than 1 km from the TCCON spectrometer site Karlsruhe. In addition, the TCCON spectrometer was operational during all days of observations with the dual-channel EM27/SUN. Therefore, the official TCCON XCO product derived from these observations can serve as the best available reference for the true column-averaged CO abundances. In addition to the standard operation mode, the high-resolution spectrometer intermittently records double-sided interferograms with the same resolution as applied by the EM27/SUN, which can be used to evaluate systematic retrieval biases introduced by the significantly different resolution of the TCCON spectrometer and the EM27/SUN.

For the pre-processing of the EM27/SUN raw data, our suite of CALPY routines was used (Frey et al., 2015). For the analysis of the EM27/SUN we applied the retrieval code PROFFIT (Hase et al., 2004). PROFFIT is in wide use in the NDACC (e.g. Sepúlveda et al., 2014; Virolainen et al., 2014; Mengistu Tsidu et al.; 2014), is in very good agreement with the official TCCON analysis (Dohe, 2013) and is also successfully applied for the analysis of spectra recorded with the EM27/SUN (Gisi et al., 2012; Frey et al., 2015). For the ~~CO~~ analysis ~~from the EM27/SUN~~ of the low-resolution spectra, the methane, water vapour, HDO, and CO a-priori profiles have been adopted from the TCCON processor. Figure 6 shows the complex spectral region containing the CO overtone band as recorded at high spectral resolution and denotes the absorption contributions from the relevant absorbers. Figure 7 shows a typical spectral fit for the spectral window 4210 to 4320 cm^{-1}, which is used for the CO analysis. Systematic fit residuals significantly larger than the noise level of the spectrometer are evident, indicating that the simulation of this crowded spectral scene shaped by numerous strong absorption lines could be improved by further progress on spectroscopic data (our fits are essentially based on HITRAN 2008, see Rothman et al., 2008). The provision of an improved and consolidated set of spectroscopic data for the spectral region under consideration here is an ongoing effort (e.g. Galli et al., 2012; Scheepmaker et al., 2013; http://seom.esa.int/page_project003.php).

Before we discuss results derived from the new spectral channel, we investigate whether the modifications performed on the prototype affected the results for the oxygen column, which is derived from the existing spectral channel. Figure 8 compares the oxygen column from the

dual-channel prototype before and after the intervention and the standard EM27/SUN used as a reference. The agreement meets our design expectations ~~excellent~~; no detectable offset as result of the dual channel implementation is found. We therefore assume that the implementation of the extension did not significantly affect the behaviour of spectrometer's primary channel. Note that a comparison of oxygen columns is a very sensitive test, as many instrumental errors tend to cancel out in the final column averaged abundances of the target species.

Next, we investigate the compatibility of ~~X~~CH_4 columns derived from the primary detector with the ~~X~~CH_4 columns from the secondary detector. CH_4 is the main absorber in the 4200 – 4320 cm^{-1} region, followed by H_2O and HDO. The CO overtone band is weak in comparison to the signatures of the other species, so CH_4 provides a more sensitive handle for revealing any instrumental issues. Figure 9 shows the ~~X~~CH_4 columns from both channels of the prototype. The two datasets are in ~~excellent~~ mutual agreement on the 0.1% level. There is a systematic offset between the two time series (scaling factor 1.0133+-0.0024), very likely due to residual inconsistencies of the spectroscopic line intensities. The standard deviation of the ratio of both time series is ~~0.092%~~ 0.104%. It should be noted that a misalignment between the primary and secondary fieldstop would induce systematic differences as function of azimuthal viewing angle. Indeed, the comparison of the two ~~XCH4~~ methane products provides a tool for detecting a misalignment of the secondary fieldstop, because a variation induced by our limited capability to simulate the spectral scene will be symmetric around local noon, whereas the fieldstop misalignment will differ between morning and afternoon as a consequence of the rotation of the image on the fieldstop as function of azimuthal viewing angle (Reichert et al., 2015). At a solar elevation angle of 20° a 0.1° displacement of the solar disc would create an error of up to 0.5% in dry air mole fractions derived from the secondary channel (solar elevation 10°: up to 1%), so this effect can easily be detected using the two methane data products and subsequently be applied for establishing a correction for XCO, if required. However, we do not observe such ~~kind of~~ a suspicious discrepancy between the two time series.

Finally, we investigate the XCO timeseries derived from the prototype. Figure 10 displays ~~the whole dataset as function of airmass~~ measurements recorded in the 15 to 33 degrees range of

solar elevation angles, the daily mean values have been scaled in order to remove the day-to-day variability. Obviously, the results are affected by an airmass dependency. The presence of such an artificial airmass dependency is a frequent problem created by our inability to simulate the observed spectral scene perfectly ~~well~~. We therefore apply a second-order polynomial (shown in Figure 10) to remove this artefact. We have located the neutral point of this correction at 25 degree solar elevation angle, which is near the average solar elevation angle of the complete dataset. Figure 10 in addition shows a strong and a weak variant of the correction, which result in significantly poorer fits to the observed data. These two ad-hoc modifications will be used in the comparison with the TCCON reference dataset for estimating the level of uncertainty introduced by the airmass correction. ~~Note that~~ The TCCON also requires the aid of empirical airmass corrections for carbon monoxide and other target species.

Figure 11 presents the XCO data as derived from the dual-channel EM27/SUN prototype in comparison to the official TCCON data product. The airmass correction clearly improves the agreement with the TCCON reference (as seen in the upper panel of Figure 11). ~~The airmass-corrected XCO data deduced from the dual-channel prototype are slightly smaller (scaling factor 0.978) than the TCCON reference and the standard deviation of the difference of the daily means is 1.1 %.~~ The XCO results deduced from the dual-channel prototype are in agreement with the TCCON reference dataset (within the statistical uncertainty of the calibration factor). The strong and weak variants of the airmass correction do somewhat affect the calibration factor of the prototype XCO. However, the resulting deviations from unity are still not significant on the 2 σ level of the statistical uncertainty. Note that apart from the empirical airmass correction and the TCCON calibration factor derived from aircraft measurements (Kiel et al., 2015b) no adjustments on the XCO derived from the prototype have been applied. The precision of an individual XCO measurement can be estimated from differences of successive measurements and amounts to 0.35 ppb.

The vertical sensitivity of the low resolution spectrometer differs somewhat from the TCCON sensitivity. This is a consequence of differing spectral resolutions, and introduces a smoothing error component in the comparison. Sensitivities for both the low-resolution spectrometer and TCCON are shown in the work by Hedelius et al., 2016, indicating that the CO sensitivity of

the low-resolution spectrometer is even superior to that of the TCCON. In this study - focused on an instrumental validation - we minimized the systematic smoothing error contribution by using the same atmospheric CO a-priori profiles as the TCCON in our spectral analysis. An in-depth quantification of the smoothing error has been performed by Kiel et al., 2015b. The authors compared TCCON results with data derived from mid-infrared spectra (with a comparable degree of mismatch of vertical sensitivities) and found smoothing error contributions of a few per cent due to different a-priori profile choices and vertical sensitivities. We have included the mid-infrared observations of XCO in the lower panel of Figure 11, because these results support our explanation of the remaining discrepancies being generated by different vertical sensitivities of the TCCON and the prototype measurements: the mid-infrared observations of XCO tend to be low compared to TCCON when the prototype results are low and high when the prototype results are high.

The demonstrated performance of the prototype indicates that the design is well suited for source attribution (Wunch et al., 2009, detected intraday XCO enhancements of up to 30 % in the Los Angeles Basin) and satellite validation (the TROPOMI accuracy and precision targets are 15% and 10%, respectively). We expect that the upcoming set of improved spectroscopic data will further improve the ~~consistency~~ reliability of XCO derived from ~~results between TCCON and the~~ low-resolution spectra (ideally rendering the airmass-depending correction obsolete).

In ~~October, 12, 2015,~~ March, 18, 2016, a larger intraday variability of XCO occurred, which has been nicely sampled by both the TCCON spectrometer and the prototype. The results are shown in Figure 12, indicating that the prototype can detect XCO ~~enhancements on the 0.5 % level~~ intraday variability in the sub-percent range.

6 Summary and Outlook

The portable EM27/SUN spectrometer is dedicated to measurements of column-averaged abundances of carbon dioxide and methane with sufficient quality for climate research. In this work, we have described a dual-channel extension of this device, which can be added in a

straightforward manner without interfering with the standard setup of the spectrometer. The second channel uses an extended InGaAs detector element and a wedged Ge filter to define a spectral bandpass beyond the spectral coverage of the standard spectrometer. It is fed via a small plane mirror which decouples parts of the beam towards a secondary detector element. This approach avoids interference with the concept of a camera-controlled tracker referenced to the fieldstop and conserves the spectral coverage and characteristics of the primary detector. The secondary detector allows the simultaneous measurement of XCO, which is a very useful tool for source characterisation, while the use of a cooled detector element can be avoided. In the second part of this work, we performed a preliminary validation of the setup by verifying that the dual-channel prototype maintains the characteristics of the standard spectrometer and by investigating the XCO data product. We showed that due to the fact that methane is the primary absorber in the spectral window used for the carbon monoxide analysis, the comparison of CH_4 columns derived from either the primary or the secondary channel can be used as a diagnostic tool for detecting a residual misalignment of the secondary fieldstop or other instrumental issues.

We plan a further in-depth characterisation of the dual-channel EM27/SUN prototype introduced here. The spectrometer is foreseen to participate in the TCCONcomp campaign funded by ESA. This campaign is scheduled for 2017, is led by University of Bremen, Germany, and BIRA (Royal Belgian Institute for Space Aeronomy), Belgium, and involves several partners contributing various promising approaches for the Sentinel 5 Precursor validation. The aim of TCCONcomp is to validate these techniques with respect to the TCCON reference instrument operated by FMI (Finnish Meteorological Institute) at the Sodankyla station, Finland.

We would like to mention that the secondary channel of the extended EM27/SUN also allows observation of HDO, opening up the possibility of also using the device for observations of water vapour isotopic variability, although the verification of the quality and information content of such data from low-resolution spectra will require careful validation efforts (for prior work based on high-resolution near-infrared spectra see Rokotyan et al., 2014). The new spectroscopic datasets under preparation in support of the Sentinel 5 Precursor mission will be a highly valuable ingredient for TCCON, ~~for~~ the spectrometer presented here and ~~for~~ any other remote sensing devices working in the 2.35 µm spectral region targeting ~~at~~ methane, carbon monoxide or water vapour isotopic composition.

Acknowledgements

We acknowledge support by the ACROSS and MOSES research infrastructures of the Helmholtz Association.

We acknowledge support by Deutsche Forschungsgemeinschaft and Open Access Publishing Fund of the Karlsruhe Institute of Technology.

We thank the anonymous referees for triggering numerous useful corrections of the original manuscript.

References

Butz, A., S. Guerlet, D. J. Jacob, D. Schepers, A. Galli, I. Aben, C. Frankenberg, J.-M. Hartmann, H. Tran, A. Kuze, G. Keppel-Aleks, G. C. Toon, D. Wunch, P. O. Wennberg, N. M. Deutscher, D. W. T. Griffith, R. Macatangay, J. Messerschmidt, J. Notholt, and T. Warneke: Toward accurate CO2 and CH4 observations from GOSAT, Geophysical Research Letters, 38(14), 2-7, doi:10.1029/2011GL047888, 2011.

Dohe, S.: Measurements of atmospheric CO_2 columns using ground-based FTIR spectra, Dissertation, Karlsruhe Institute for Technolgy (KIT), Germany, 2013.

Frey, M., Hase, F., Blumenstock, T., Groß, J., Kiel, M., Mengistu Tsidu, G., Schäfer, K., Sha, M. K., and Orphal, J.: Calibration and instrumental line shape characterization of a set of portable FTIR spectrometers for detecting greenhouse gas emissions, Atmos. Meas. Tech., 8, 3047-3057, 2015, doi:10.5194/amt-8-3047-2015.

Galli, A., A. Butz, R. A. Scheepmaker, O. Hasekamp, J. Landgraf, P. Tol, D. Wunch, N. M. Deutscher, G. C. Toon, P. O. Wennberg, D. W. T. Griffith, and I. Aben: CH_4, CO, and H_2O spectroscopy for the Sentinel-5 Precursor mission: an assessment with the Total Carbon Column Observing Network measurements, Atmospheric Measurement Techniques, 5(6), 1387-1398, doi:10.5194/amt-5-1387-2012.

Gisi, M., Hase, F., Dohe, S., Blumenstock, T., Simon, A., and Keens, A.: XCO_2-measurements with a tabletop FTS using solar absorption spectroscopy, Atmos. Meas. Tech., 5, 2969-2980, 2012, doi:10.5194/amt-5-2969-2012.

Gisi, M., Hase, F., Dohe, S., and Blumenstock, T.: Camtracker: A new camera controlled high precision solar tracker system for FTIR-spectrometers, Atmos. Meas. Tech., 4, 47-54, 2011, doi:10.5194/amt-4-47-2011.

Hase, F., Hannigan, J., Coffey, M., Goldman, A., Höpfner, M., Jones, N., Rinsland, C., and Wood, S.: Intercomparison of retrieval codes used for the analysis of high resolution, ground-based FTIR measurements, J. Quant. Spectrosc. Ra., 87, 25–52, 2004, doi:10.1016/j.jqsrt.2003.12.008.

Hase, F., Frey, M., Blumenstock, T., Groß, J., Kiel, M., Kohlhepp, R., Mengistu Tsidu, G., Schäfer, K., Sha, M. K., and Orphal, J.: Application of portable FTIR spectrometers for detecting greenhouse gas emissions of the major city Berlin, Atmos. Meas. Tech., 8, 3059-3068, 2015, doi:10.5194/amt-8-3059-2015.

~~Hedelius, J., et al., 2016; manuscript in preparation for AMTD (submission scheduled for Jan 15, 2016).~~

Hedelius, J. K., C. Viatte, D. Wunch, C. Roehl, G. C. Toon, J. Chen, T. Jones, S. C. Wofsy, J. E. Franklin, H. Parker, M. K. Dubey, and P. O. Wennberg, "Assessment of errors and biases in retrievals of XCO2, XCH4, XCO, and XN2O from a 0.5 cm−1 resolution solar viewing spectrometer", AMTD, 2016

Heymann, J., M. Reuter, M. Hilker, M. Buchwitz, O. Schneising, H. Bovensmann, J. P. Burrows, A. Kuze, H. Suto, N. M. Deutscher, M. K. Dubey, D. W. T. Griffith, F. Hase, S. Kawakami, R. Kivi, I. Morino, C. Petri, C. Roehl, M. Schneider, V. Sherlock, R. Sussmann, V. a. Velazco, T. Warneke, and D. Wunch: Consistent satellite XCO_2 retrievals from SCIAMACHY and GOSAT using the BESD algorithm, Atmos. Meas. Tech., 8(7), 2961–2980, 2015, doi:10.5194/amt-8-2961-2015.

Inoue, M., I. Morino, O. Uchino, T. Nakatsuru, Y. Yoshida, T. Yokota, D. Wunch, P. O. Wennberg, C. M. Roehl, D. W. T. Griffith, V. A. Velazco, N. M. Deutscher, T. Warneke, J. Notholt, J. Robinson, V. Sherlock, F. Hase, T. Blumenstock, M. Rettinger, R. Sussmann, E. Kyrö, R. Kivi, K. Shiomi, S. Kawakami, M. De Mazière, S. G. Arnold, D. G. Feist, E. A. Barrow, J. Barney, M. Dubey, M. Schneider, L. Iraci, J. R. Podolske, P. Hillyard, T. Machida, Y. Sawa, K. Tsuboi, H. Matsueda, C. Sweeney, P. P. Tans, A. E. Andrews, S. C. Biraud, Y.

Fukuyama, J. V. Pittman, E. A. Kort, and T. Tanaka: Bias corrections of GOSAT SWIR XCO2 and XCH4 with TCCON data and their evaluation using aircraft measurement data, Atmos. Meas. Tech. Discuss., doi:10.5194/amt-2015-366, in review, 2016.

Keppel-Aleks, G., G. C. Toon, P. O. Wennberg, and N. M. Deutscher: Reducing the impact of source brightness fluctuations on spectra obtained by Fourier-transform spectrometry, Applied Optics, 46(21), 4774-9, 2007.

Kiel, M., D. Wunch, P. O. Wennberg, G. C. Toon, F. Hase, and T. Blumenstock: Improvement of the retrieval used for Karlsruhe TCCON data, under review for AMT, 2015a.

Kiel, M. , F. Hase, T. Blumenstock, and O. Kirner: Comparison of XCO abundances from the Total Carbon Column Observing Network and the Network for the Detection of Atmospheric Composition Change measured in Karlsruhe, submitted to AMT, 2015b.

Klappenbach, F., Bertleff, M., Kostinek, J., Hase, F., Blumenstock, T., Agusti-Panareda, A., Razinger, M., and Butz, A.: Accurate mobile remote sensing of XCO_2 and XCH_4 latitudinal transects from aboard a research vessel, Atmos. Meas. Tech., 8, 5023-5038, 2015, doi:10.5194/amt-8-5023-2015.

Lindenmaier, R., M. K. Dubey, B. G. Henderson, Z. T. Butterfield, J. R. Herman, T. Rahn, and S. Lee: Multiscale observations of CO_2, $^{13}CO_2$, and pollutants at Four Corners for emission verification and attribution, Proceedings of the National Academy of Sciences of the United States of America, 111(23), 8386–8391, 2014, doi:10.1073/pnas.1321883111.

~~Lindqvist, H., C. W. O'Dell, S. Basu, H. Boesch, F. Chevallier, N. Deutscher, L. Feng, B. Fisher, F. Hase, M. Inoue, R. Kivi, I. Morino, P. I. Palmer, R. Parker, M. Schneider, R. Sussmann, and Y. Yoshida: Does GOSAT capture the true seasonal cycle of carbon dioxide?, Atmos. Chem. Phys., 15(22), 13023–13040, 2015, doi:10.5194/acp-15-13023-2015.~~

Mengistu Tsidu, G., Blumenstock, T., and Hase, F.: Observations of precipitable water vapour over complex topography of Ethiopia from ground-based GPS, FTIR, radiosonde and ERA-Interim reanalysis, Atmos. Meas. Tech. Discuss., 7, 9869-9915, 2014, doi:10.5194/amtd-7-9869-2014.

Messerschmidt, J., Parazoo, N., Wunch, D., Deutscher, N. M., Roehl, C., Warneke, T., and Wennberg, P. O.: Evaluation of seasonal atmosphere–biosphere exchange estimations with TCCON measurements, Atmos. Chem. Phys., 13, 5103-5115, 2013, doi:10.5194/acp-13-5103-2013.

Petri, C., Warneke, T., Jones, N., Ridder, T., Messerschmidt, J., Weinzierl, T., Geibel, M., and Notholt, J.: Remote sensing of CO_2 and CH_4 using solar absorption spectrometry with a low resolution spectrometer, Atmos. Meas. Tech., 5, 1627-1635, 2012, doi:10.5194/amt-5-1627-2012.

Reichert, A., Hausmann, P., and Sussmann, R.: Pointing errors in solar absorption spectrometry – correction scheme and its validation, Atmos. Meas. Tech., 8, 3715-3728, 2015, doi:10.5194/amt-8-3715-2015.

Rokotyan, N. V., V. I. Zakharov, K. G. Gribanov, M. Schneider, F.-M. Bréon, J. Jouzel, R. Imasu, M. Werner, M. Butzin, C. Petri, T. Warneke, and J. Notholt: A posteriori calculation of δ18O and δD in atmospheric water vapour from ground-based near-infrared FTIR retrievals of H216O, H218O, and HD16O, Atmos. Meas. Tech., 7(8), 2567–2580, doi:10.5194/amt-7-2567-2014, 2014.

Rothman, L. S., Gordon, I. E., Barbe, A., Benner, D. C., Bernath, P. F., Birk, M., Boudon, V., Brown, L. R., Campargue, A., Champion, J.-P., Chance, K., Coudert, L. H., Dana, V., Devi, V. M., Fally, S., Flaud, J.-M., Gamache, R. R., Goldman, A., Jacquemart, D., Kleiner, I., Lacome, N., Lafferty,W. J., Mandin, J.-Y., Massie, S. T., Mikhailenko, S. N., Miller, C. E.,

Moazzen-Ahmadi, N., Naumenko, O. V., Nikitin, A. V., Orphal, J., Perevalov, V. I., Perrin, A., Predoi-Cross, A., Rinsland, C. P., Rotger, M., Simeckova, M., Smith, M. A. H., Sung, K., Tashkun, S. A., Tennyson, J., Toth, R. A., Vandaele, A. C., and Vander Auwera, J.: The HITRAN 2008 molecular spectroscopic database, J. Quant. Spectrosc. Ra., 110, 533–572, doi:10.1016/j.jqsrt.2009.02.013, 2009.

Scheepmaker, R. A., Frankenberg, C., Galli, A., Butz, A., Schrijver, H., Deutscher, N. M., Wunch, D., Warneke, T., Fally, S., and Aben, I.: Improved water vapour spectroscopy in the 4174–4300 cm^{-1} region and its impact on SCIAMACHY HDO/H_2O measurements, Atmos. Meas. Tech., 6, 879-894, doi:10.5194/amt-6-879-2013, 2013.

Sepúlveda, E., M. Schneider, F. Hase, S. Barthlott, D. Dubravica, O. E. García, A. Gomez-Pelaez, Y. González, J. C. Guerra, M. Gisi, R. Kohlhepp, S. Dohe, T. Blumenstock, K. Strong, D. Weaver, M. Palm, A. Sadeghi, N. M. Deutscher, T. Warneke, J. Notholt, N. Jones, D. W. T. Griffith, D. Smale, G. W. Brailsford, J. Robinson, F. Meinhardt, M. Steinbacher, T. Aalto, and D. Worthy: Tropospheric CH_4 signals as observed by NDACC FTIR at globally distributed sites and comparison to GAW surface in-situ measurements, Atmos. Meas. Tech., 7, 2337-2360, 2014, doi:10.5194/amt-7-2337-2014.

Virolainen, Y., Timofeyev, Y., Polyakov, A., Ionov, D., and Poberovsky, A: Intercomparison of satellite and ground-based measurements of ozone, NO_2, HF, and HCl near Saint Petersburg, Russia, International Journal of Remote Sensing, 35:15, 5677-5697, 2014, doi: 10.1080/01431161.2014.945009.

Wunch, D., G.C. Toon, J.-F.L. Blavier, R.A. Washenfelder, J. Notholt, B.J. Connor, D.W.T. Griffith, V. Sherlock, P.O. Wennberg: The Total Carbon Column Observing Network. Phil. Trans. R. Soc. A , 2011, 369, doi:10.1098/rsta.2010.0240.

Wunch, D., P. O. Wennberg, G. C. Toon, G. Keppel-Aleks, and Y. G. Yavin. Emissions of greenhouse gases from a North American megacity, Geophysical Research Letters, 36(15), 1-5, 2009, doi:10.1029/2009GL039825.

Table 1. Overview of measurement days before and after modification of the spectrometer. The number of spectra used in the comparison is indicated. The modification of the prototype was performed before 151012. NIR denotes spectra recorded in the near infrared for the TCCON analysis, MIR denotes mid-infrared observations of the fundamental band of CO as used for the NDACC analysis.

Date (JJMMDD)	Number of spectra recorded with the EM27/SUN selected for modification (S/N0039)	Number of spectra recorded with the EM27/SUN used as a reference (S/N0037)	Number of spectra recorded with the 125HR spectrometer (NIR / MIR)
150518	368	369	n/a
150521	282	276	n/a
150702	465	477	n/a
150703	472	473	n/a
150706	342	344	n/a
150710	338	330	n/a
150831	387	400	n/a
-	Modification performed	-	-
151012	206	not operated	86 / 4
151026	186	201	40 / 3
151105	136	173	72 / 4
151110	83	114	33 / 2
151111	103	107	20 / 2
151116	79	63	71 / 3
160318	322	297	124 / 7

1

2

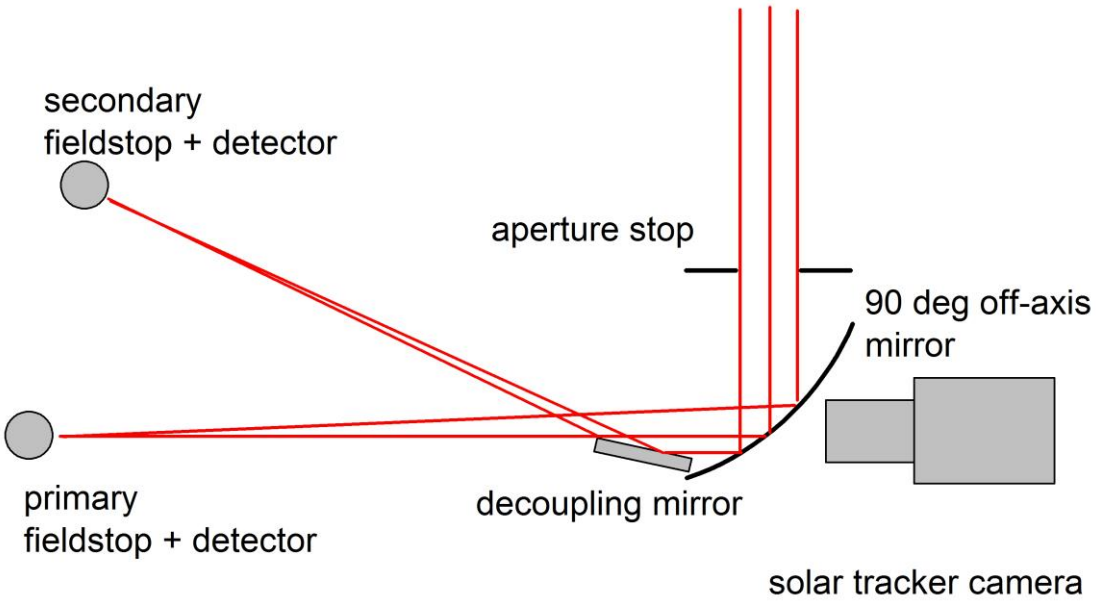

Figure 1. : Schematic drawing of the detector branch of the extended EM27/SUN. The camera is located above the drawing plane and images the primary fieldstop. For clarity, the camera position has been shifted to the right in the drawing, it actually is located above the off-axis mirror.

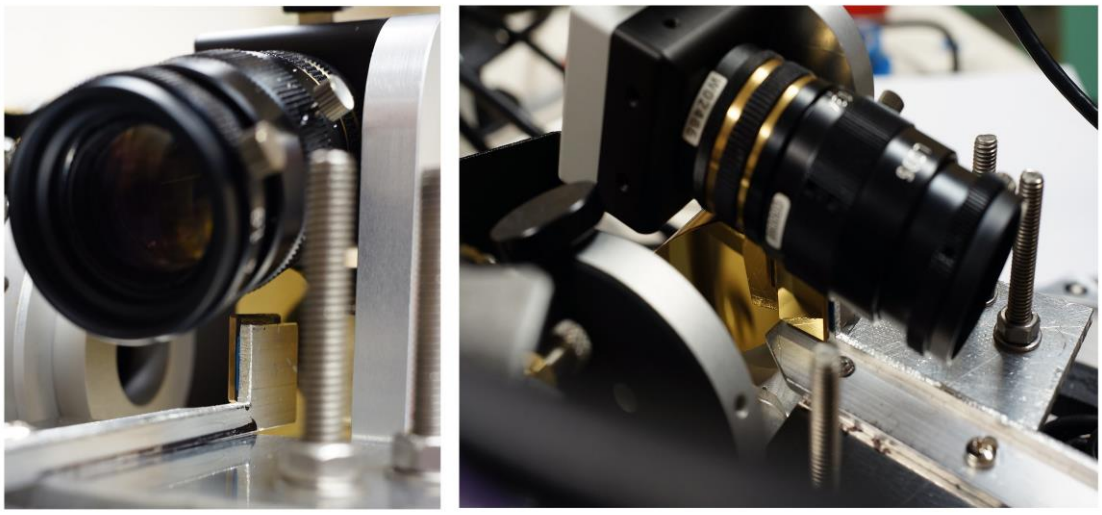

Figure 2. Close-up of the plane mirror used for decoupling of the secondary beam. Figure 2a (left side) shows the support arm which carries the mirror. The mirror itself is seen from the back. On the left, parts of the circular mounting of the adjustable iris are seen. Behind the contours of the plane mirror, the larger off axis paraboloid is located. Above the mirror, the camera used for the camera-controlled solar tracker is located. Figure 2b (right side) offers a different perspective: below the camera, the front side of the plane mirror is seen. The frame of the iris is seen from the back.

Figure 3. In the front, the image of an artificial source covering about the same angle as the solar disc is seen on the primary field stop. The support for the secondary field stop is mounted on the primary detector. The secondary field stop itself is realized as a 0.8 mm hole in the aluminium sheet. The image of the source on the secondary field stop is seen to the upper right from the centre of the image. The final alignment of the image position with

respect to the position of the secondary field stop is performed by fine adjustment of the plane mirror.

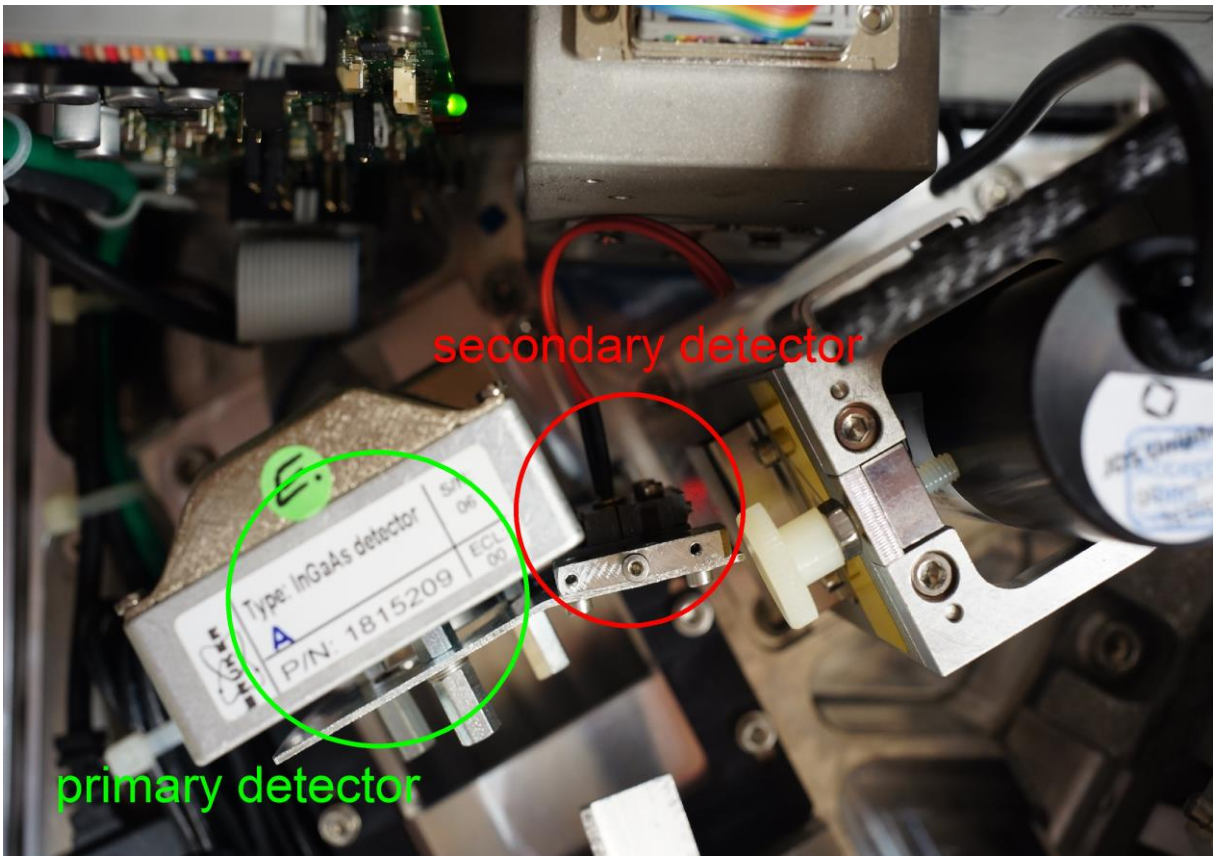

Figure 4. This image provides a top view of the detector units. The primary detector remains in its standard detector box, the supporting structure for the secondary field stop is mounted on the box of the primary detector. The secondary detector and the Ge filter are accommodated in a separate holder, which can be adjusted laterally with respect to the field stop.

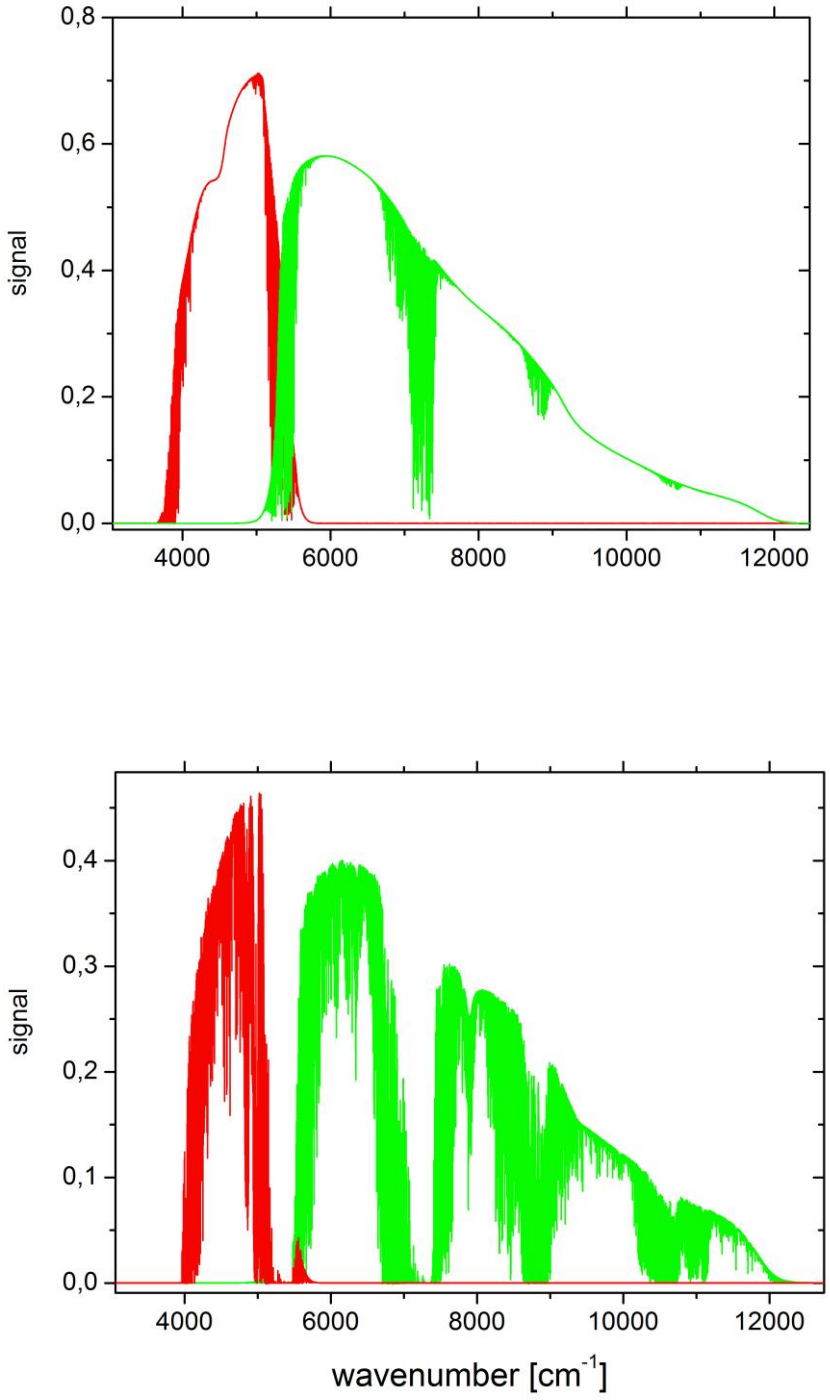

Figure 5. Lamp spectrum (top) and solar spectrum (bottom) recorded with the dual channel prototype. The primary detector covers the spectral section observed with the standard EM27/SUN, the secondary detector covers the 4000 – 5500 cm^{-1} region.

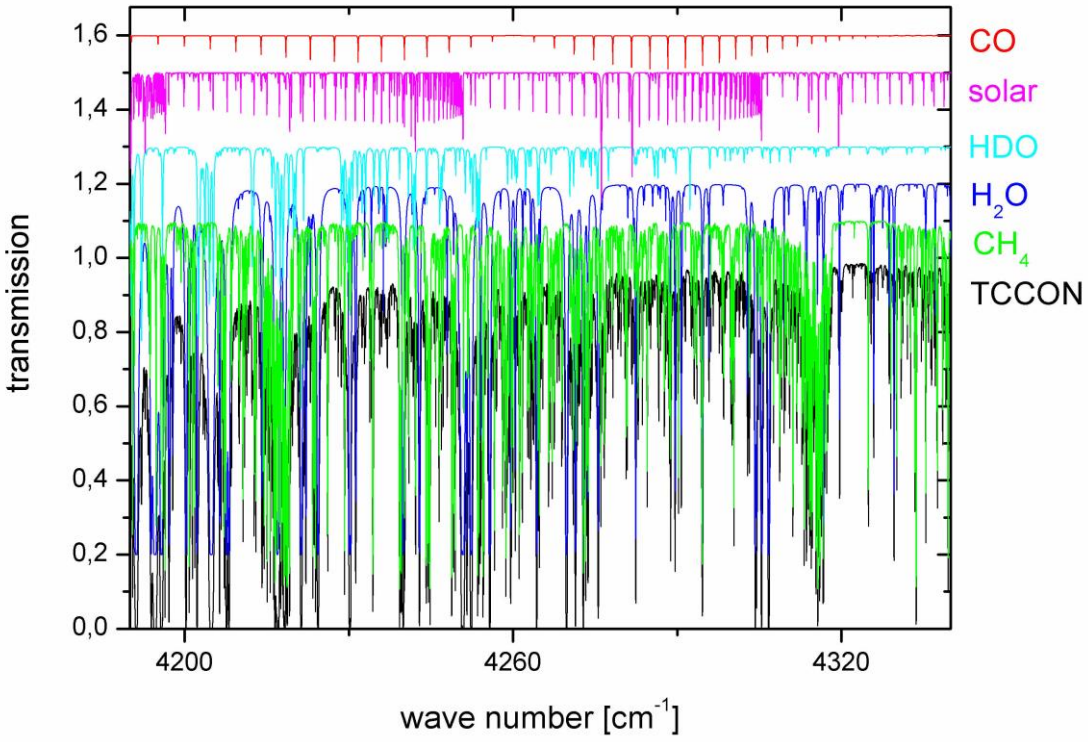

1

2

3 Figure 6. Spectrum simulated for TCCON resolution showing the relevant absorption features
4 in the spectral region under consideration.

5

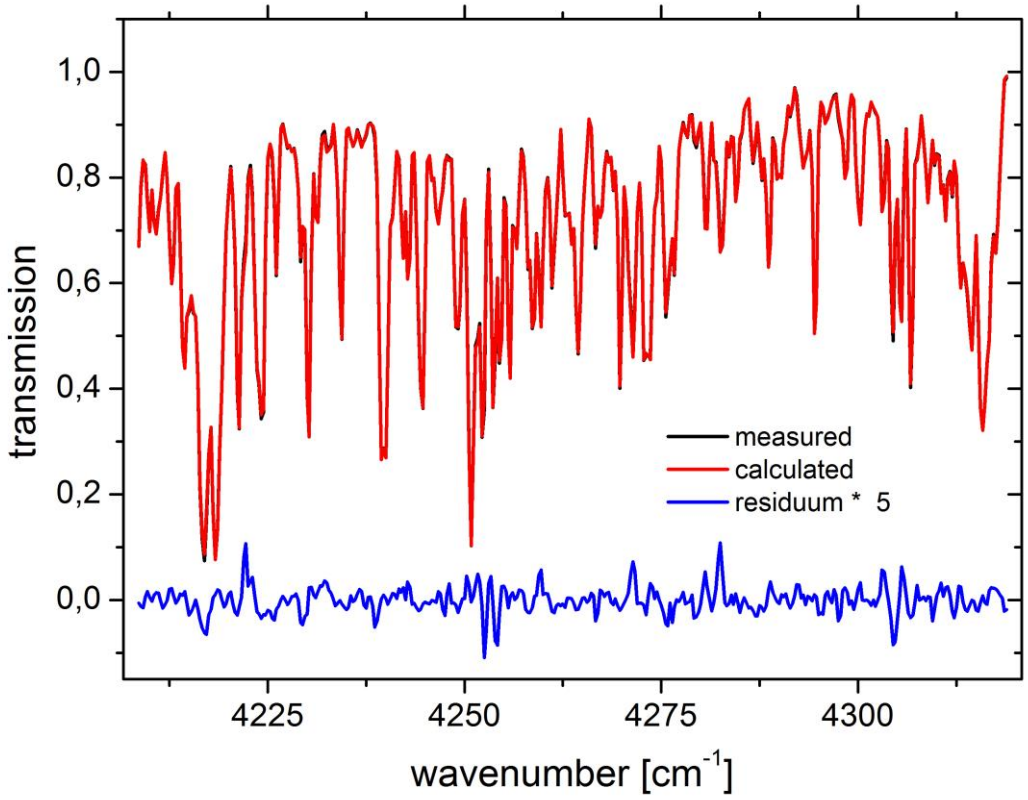

Figure 7. Typical spectral fit for the selected CO fitting region (4210 – 4320 cm^{-1}). Interfering species are CH_4, H_2O and HDO.

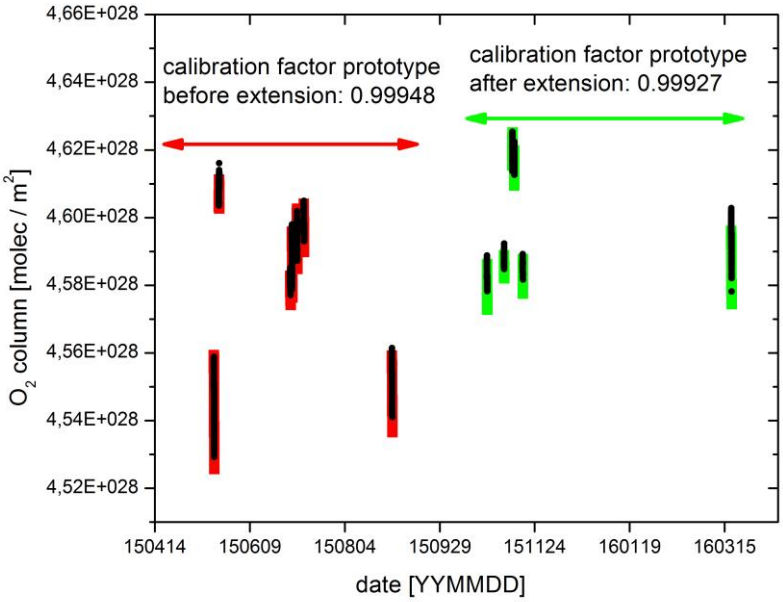

1

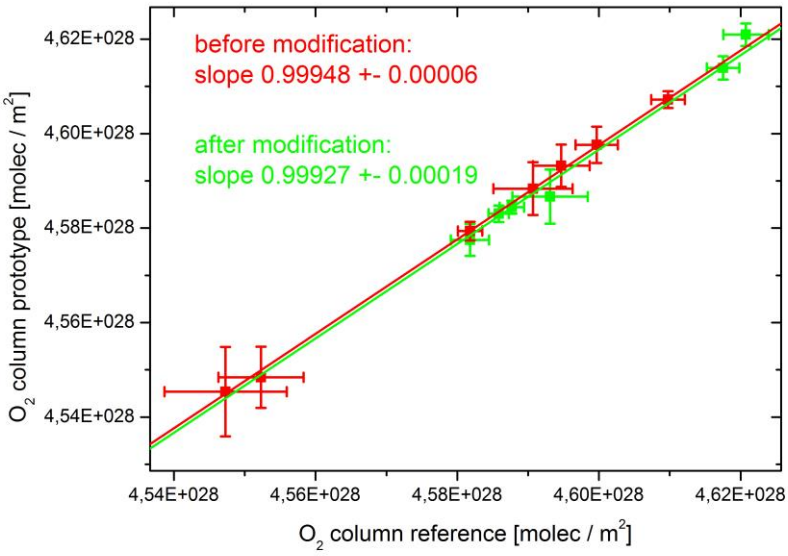

2

3 Figure 8. Total column amounts of molecular oxygen measured with the EM27/SUN used as
4 a reference (data in black) and the prototype before and after the implementation (before: red,
5 after: green) of the secondary channel. The implemented extension did not affect the
6 characteristics of the prototype. Upper panel: time series of the O_2 column amounts as
7 recorded with the reference spectrometer and the prototype. Lower panel: Mean daily O_2
8 column amounts as recorded with the prototype as function of the values recorded with the

reference spectrometer. The error bars shown are the standard deviation of the intraday scatter. The calibration factors before and after the modification of the prototype are in mutual agreement.

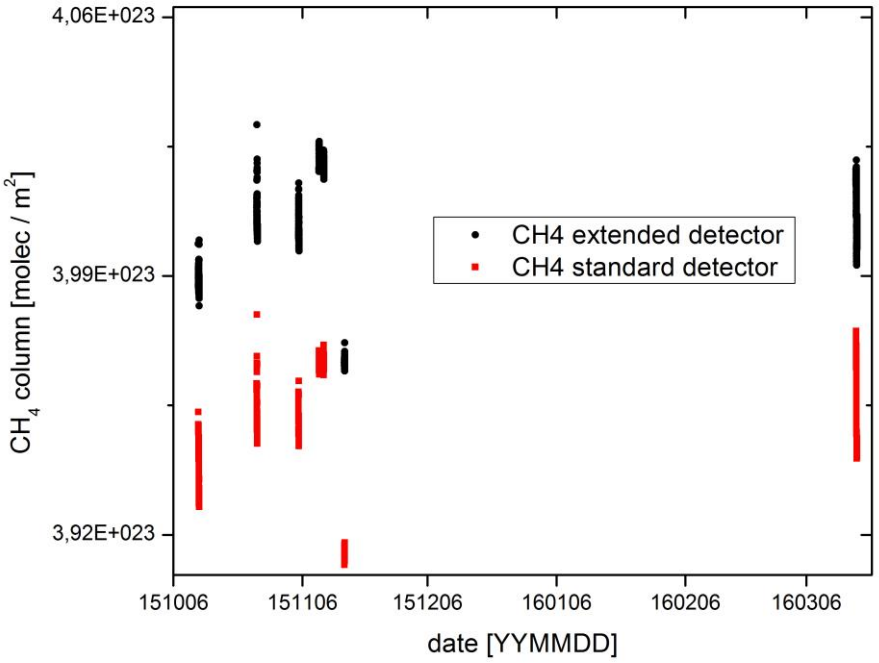

1

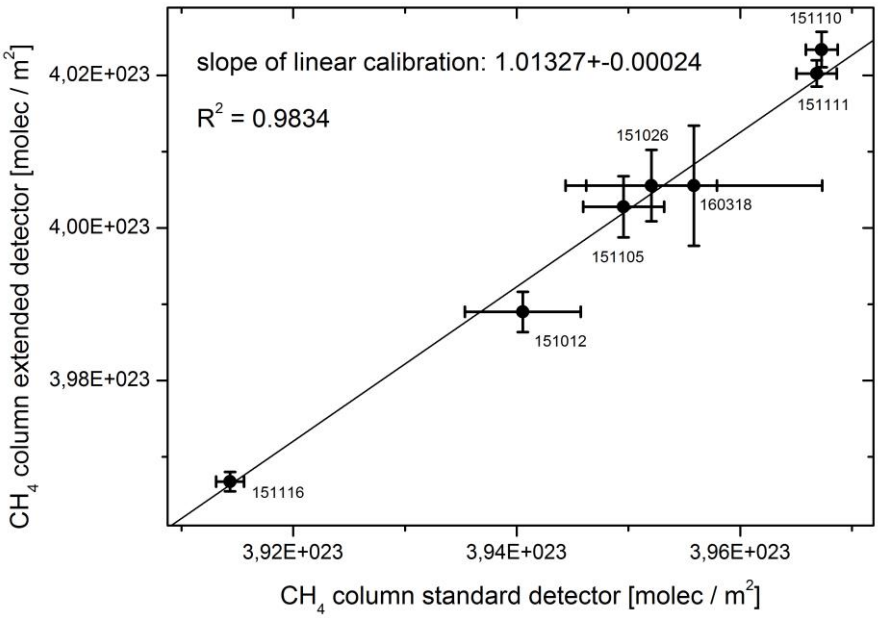

2

3 Figure 9. Comparison of methane column amounts as derived from the primary and secondary
4 spectral channel. Upper panel: time series of methane columns. Lower panel: daily mean
5 values of methane columns derived from the extended detector as function of the methane

columns derived from the standard detector. The error bars are the standard deviations of the intraday scatter. A linear fit of the calibration factor suggests a systematic spectroscopic offset of 1.013. There is no indication of a drift of the instrumental characteristics of the extended detector results with respect to the standard detector.

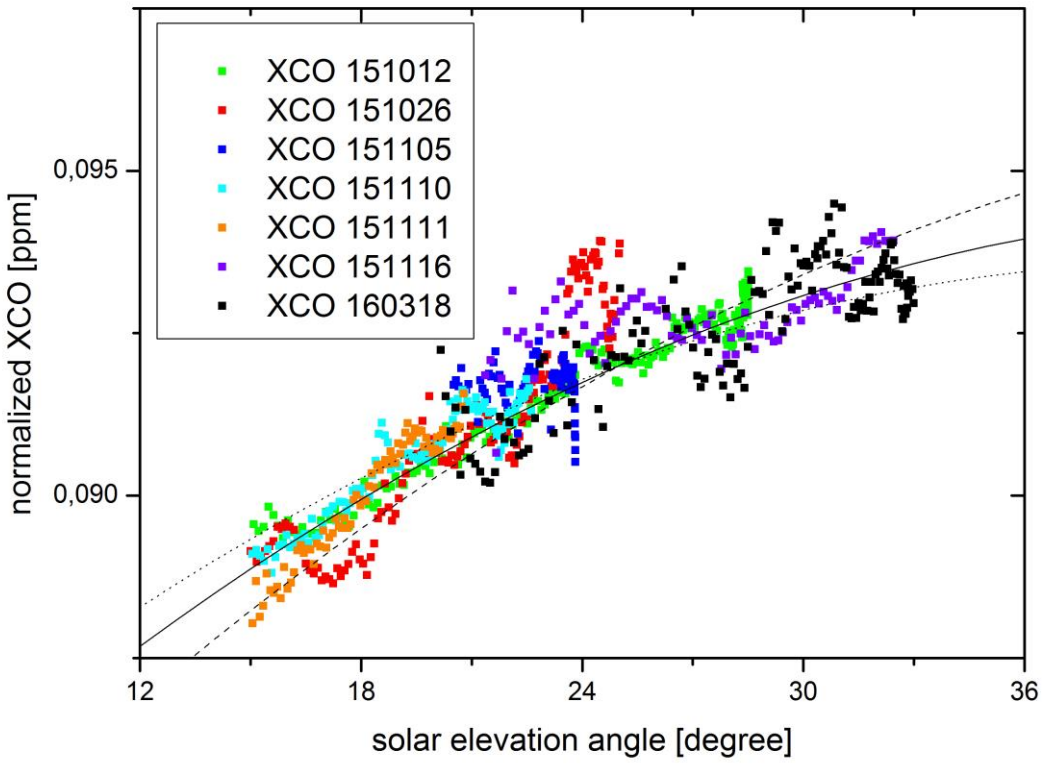

Figure 10. Apparent airmass dependency of the XCO data observed with the dual-channel prototype. For the airmass correction, we applied a second order polynomial fit, choosing 25 degree as the neutral point. For establishing the correction, spectra taken between 15 degree and 33 degree SEA have been taken into account. This choice results in the functional form (1 + 0.0027 * (SEA - 25°) - 0.00007 * (SEA - 25°)^2), wherein SEA denotes the solar elevation angle (solid curve). For estimating the uncertainty introduced by the airmass correction when comparing the prototype XCO results with the TCCON, the linear term of the fit has been increased to 0.0034 (overcorrection, dashed curve) and decreased to 0.0022 (undercorrection, dotted curve).

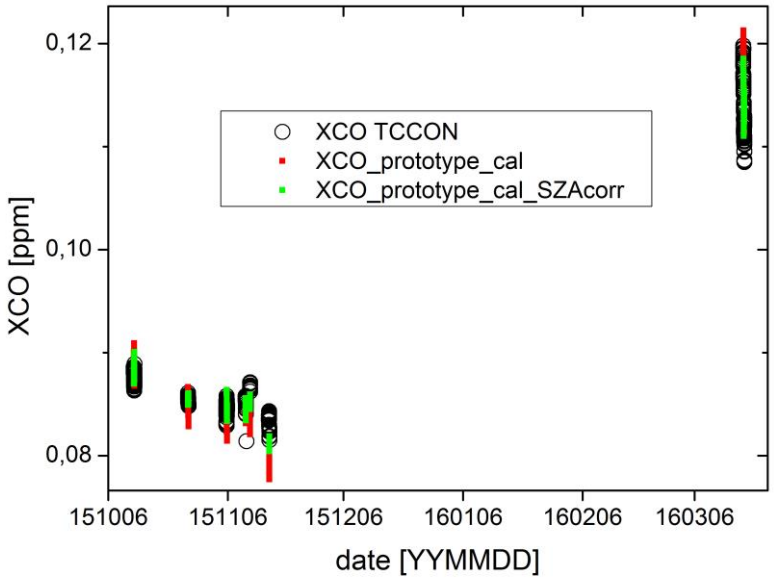

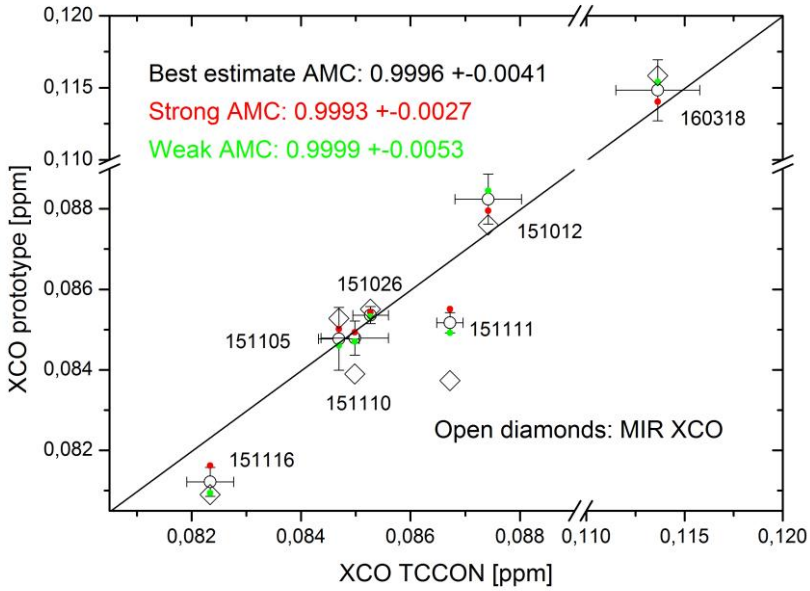

Figure 11. XCO deduced from the dual-channel prototype and the TCCON site Karlsruhe. Upper panel: time series of XCO. Lower panel: XCO values measured with the prototype as function of the collocated TCCON XCO values (AMC denotes air mass correction). The error bars are the standard deviations of the intraday scatter. In the upper panel, all available

TCCON values have been taken into account, whereas for the calculation of the statistics shown in the lower panel, the TCCON measurements have been restricted to the observing hours of the prototype, because the intraday variability is not negligible in case of XCO. As indicated by the calibration factors, the choice of the airmass correction does not critically impact the level of agreement found between the prototype and the TCCON XCO observations. The lower panel of the figure in addition shows XCO results derived from high-resolution mid-infrared spectra (open diamonds), analysed as described by Kiel et al., 2015b.

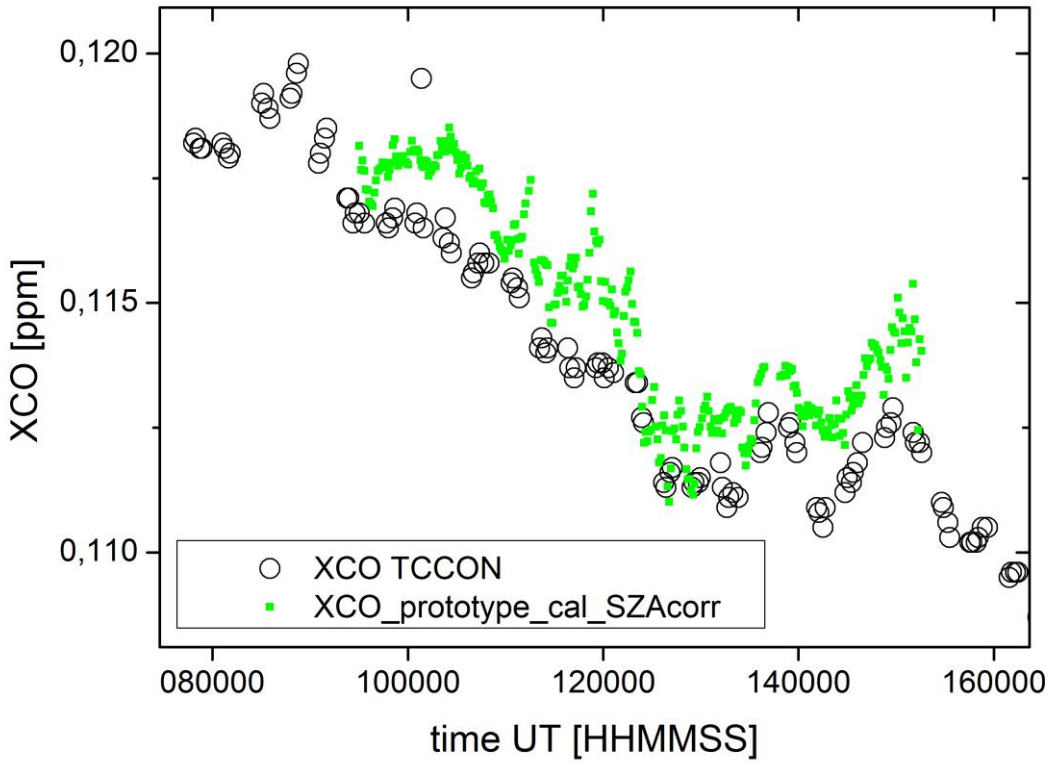

Figure 12. XCO intraday variability as observed during March, 18, 2016, by the TCCON spectrometer and the dual-channel prototype.